

# Enhancing Spin-Transport Characteristics, Spin-Filtering Efficiency, and Negative Differential Resistance in Exchange-Coupled Dinuclear Co(II) Complexes for Molecular Spintronics Applications

Rupesh Kumar Tiwari, Rizwan Nabi, Rameshwar L. Kumawat, Biswarup Pathak,\* and Gopalan Rajaraman\*



Cite This: <https://doi.org/10.1021/acs.inorgchem.3c03200>



Read Online

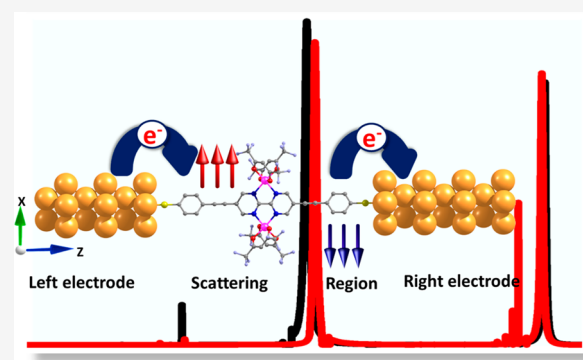
ACCESS |

Metrics & More

Article Recommendations

Supporting Information

**ABSTRACT:** Single-molecule spintronics, where electron transport occurs via a paramagnetic molecule, has gained wide attention due to its potential applications in the area of memory devices to switches. While numerous organic and some inorganic complexes have been employed over the years, there are only a few attempts to employ exchange coupled dinuclear complexes at the interface, and the advantage of fabricating such a molecular spintronics device in the observation of switchable Kondo resonance was demonstrated recently in the dinuclear  $[\text{Co}_2(\text{L})(\text{hfac})_4]$  (**1**) complex (Wagner et al., *Nat. Nanotechnol.* **2013**, *8*, 575–579). In this work, employing an array of theoretical tools such as density functional theory (DFT), the *ab initio* CASSCF/NEVPT2 method, and DFT combined with nonequilibrium Green Function (NEGF) formalism, we studied in detail the role of magnetic coupling, ligand field, and magnetic anisotropy in the transport characteristics of complex **1**. Particularly, our calculations not only reproduce the current–voltage ( $I$ – $V$ ) characteristics observed in experiments but also unequivocally establish that these arise from an exchange-coupled singlet state that arises due to antiferromagnetic coupling between two high-spin Co(II) centers. Further, the estimated spin Hamiltonian parameters such as  $J$ ,  $g$  values, and  $D$  and  $E/D$  values are only marginally altered for the molecule at the interface. Further, the exchange-coupled state was found to have very similar transport responses, despite possessing significantly different geometries. Our transport calculations unveil a new feature of the negative differential resistance (NDR) effect on **1** at the bias voltage of 0.9 V, which agrees with the experimental  $I$ – $V$  characteristics reported. The spin-filtering efficiency ( $SFE$ ) computed for the spin-coupled states was found to be only marginal ( $\sim 25\%$ ); however, if the ligand field is fine-tuned to obtain a low-spin Co(II) center, a substantial  $SFE$  of 44% was noted. This spin-coupled state also yields a very strong NDR with a peak-to-valley ratio (PVR) of  $\sim 56$  - a record number that has not been witnessed so far in this class of compounds. Additionally, we have established further magnetostructural-transport correlations, providing valuable insights into how microscopic spin Hamiltonian parameters can be associated with  $SFE$ . Several design clues to improve the spin-transport characteristics,  $SFE$  and NDR in this class of molecule, are offered.



Our transport calculations unveil a new feature of the negative differential resistance (NDR) effect on **1** at the bias voltage of 0.9 V, which agrees with the experimental  $I$ – $V$  characteristics reported. The spin-filtering efficiency ( $SFE$ ) computed for the spin-coupled states was found to be only marginal ( $\sim 25\%$ ); however, if the ligand field is fine-tuned to obtain a low-spin Co(II) center, a substantial  $SFE$  of 44% was noted. This spin-coupled state also yields a very strong NDR with a peak-to-valley ratio (PVR) of  $\sim 56$  - a record number that has not been witnessed so far in this class of compounds. Additionally, we have established further magnetostructural-transport correlations, providing valuable insights into how microscopic spin Hamiltonian parameters can be associated with  $SFE$ . Several design clues to improve the spin-transport characteristics,  $SFE$  and NDR in this class of molecule, are offered.

## INTRODUCTION

Molecular spintronics is one of the fascinating areas of electronic devices. Internal degree of freedom initiates electron transport through a specific magnetic single-molecule spintronic device by applying an external bias voltage across the leads.<sup>1,2</sup> With the advancement in the technological areas on par with fundamental physics, the spin degree of freedom of the electronics has been applied in the spintronic devices.<sup>3</sup> The electron current is composed of spin-up and spin-down carriers, which, in turn, carry information encoded in their spin state and thus behave differently with an externally applied magnetic field. This information, which is encoded in spins, persists even after the magnetic field is removed; thus, such devices can be manipulated without external magnetic fields, and the information can be written using low energies.

Spintronics exploits this behavior of these devices for their applications in device makeup. In this regard, many efforts are now being applied to develop spintronic devices that can preserve and exploit quantum coherence. Recently, Sham and co-workers reported a spin-based logic in semiconductors where spin accumulation is used as a basis of the semiconductor in computer circuits.<sup>4</sup> Shi and co-workers also

**Received:** September 12, 2023

**Revised:** November 3, 2023

**Accepted:** November 21, 2023

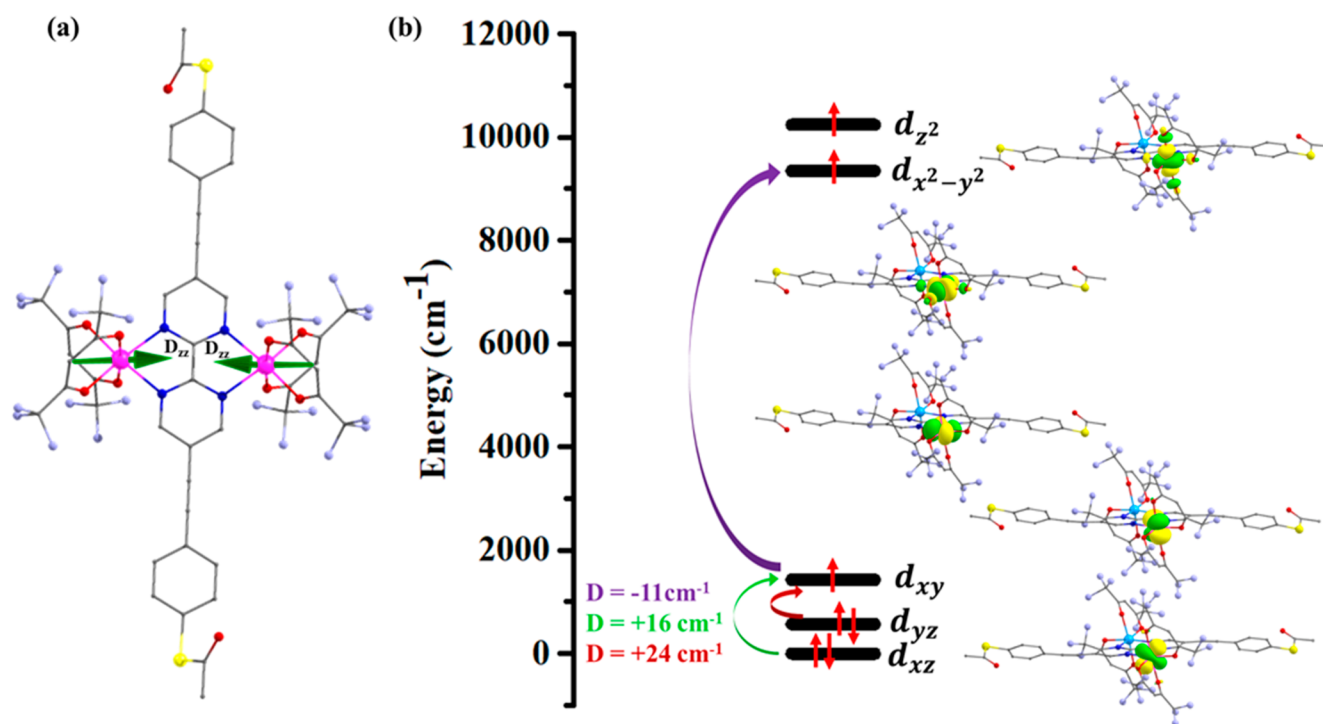


**Figure 1.** (a) DFT optimized structure of  ${}^1\mathbf{I}_{\text{hshs}}$ . The green arrows show the  $D_{zz}$  direction. (b) *Ab initio* CASSCF computed AILFT splitting diagram of the Co(II) sites for complex  ${}^1\mathbf{I}_{\text{hshs}}$ . Color code: pink, Co; yellow, S; light blue, F; red, O; blue, N; gray, C. Hydrogen atoms have been omitted for clarity.

reported the injection, transport, and detection of spin-polarized carriers in a spin valve where an organic semiconductor is used as the spacer layer.<sup>5</sup> New applications such as organic light-emitting diodes (OLEDs) and organic transistors are explored using organic molecules.<sup>6</sup>

In spintronics, the use of single-molecule magnets (SMMs) is of great interest as they show bulk magnetic properties such as slow magnetic relaxation, magnetic hysteresis, and quantum properties like quantum coherence and quantum tunnelling of magnetization at a nanoscale level, all of which are appealing for high-density storage and memory devices.<sup>7–11</sup> Incorporation of paramagnetic transition metal molecules in spin transistors provides a new robust technique because the orbital and spin degrees of freedom can be controlled through established chemistry. Many transition metal complexes such as  $\text{Mn}_{12}$ ,  $\text{Mn}_4$ ,  $\text{Mn}_6$ , and  $\text{Fe}_4$  have been explored for molecular spintronic devices.<sup>12–17</sup> Some spin-crossover (SCO) systems, such as a mononuclear hexacoordinated  $\text{Fe}^{\text{II}}$  complex, have also been studied because of the ability to switch the molecule between high spin to low spin.<sup>18</sup> As far as the application of the metal complexes as spintronic devices is concerned, it is a well-known fact that the complexes which show SCO behavior are the best candidates among all other complexes to be used as spin filtering devices.<sup>19</sup> This is probably because such complexes can easily switch between two states (low-spin to high-spin state) such that either of the states can yield a better path for the transmission of the high current density through either the spin-up ( $\alpha$ ) or spin-down ( $\beta$ ) channel. This, in turn, leads to the high spin-filtering efficiency (*SFE*) of the device obtained from such complexes. Further, the spin on the SCO complexes can be controlled by various external stimuli such as light, pressure, temperature, and electric and magnetic fields, offering further advantages for multifunctional materials.<sup>20,21</sup> Thus, such complexes can be richly exploited for the

development of electronic, spintronic, high-density data storage, nanoscale electronic, and single-molecule devices. Many cobalt (Co) and iron (Fe) based complexes have been reported to behave like SCO complexes.<sup>22</sup> Recently, Yang et al. have reported a  $\text{Fe}^{\text{II}}$  SCO complex,  $[\text{Fe}(\text{qsal}-\text{Cl})_2]$  (qsal = quinolylsalicylaldimine), studied its transport properties using a combination of density functional theory (DFT) and the nonequilibrium Green's function (NEGF) formalism, and reported a perfect spin filtering device yielding *SFE* close to 100% for the  $S = 2$  spin state with  $\beta$ -current carriers as the major channel for transport.<sup>19</sup> Further, Ruiz and co-workers have reported a  $\text{Fe}^{\text{II}}$  SCO complex, *trans*- $[\text{Fe}(\text{tzpy})_2(\text{NCS})_2]$  (tzpy = 3-(2-pyridyl)[1,2,3]triazolo[1,5-*a*]pyridine, NCS = isothiocyanato), with the *SFE* of 100% and a dominating  $\beta$ -current carrier.<sup>18</sup> Other than  $\text{Fe}^{\text{II}}$  complexes,  $\text{Co}^{\text{II}}$  mononuclear complexes were also reported to exhibit SCO phenomena between a low-spin (*ls*)  $t_{2g}^6e_g^1$  ( $S = 1/2$ ) to high-spin (*hs*)  $t_{2g}^5e_g^2$  ( $S = 3/2$ ) and have been reported to yield superior *SFEs*.<sup>23–26</sup> Despite  $\text{Fe}^{\text{II}}/\text{Co}^{\text{II}}$  systems being robust toward SCO properties, retaining the SCO characteristics at the interface is often challenging as the nature of the metal–ligand interaction, which is very delicate for the observation of SCO often altered at the interface. An alternative approach to such SCO systems has been explored with the  $[\text{Co}_2(\text{L})(\text{hfac})_4]$  (**1**) (here L = 5,5'-di(4'',4'''-di-S,S'-thiophenylethynyl)-2,2'-bipyrimidine and hfac = hexafluoroacetylacetonato) complex. In this particular complex, the two  $\text{Co}(\text{II})$  centers exhibit exchange coupling. External bias-voltage manipulation has been successfully employed to switch between these exchange-coupled states, a behavior akin to the observed SCO phenomena.<sup>27</sup> As exchange coupling in polynuclear complexes is more robust and can be retained at the interface, such molecular clusters offer a greater chance of developing a spin-filter with greater efficiency for device fabrication—a challenge

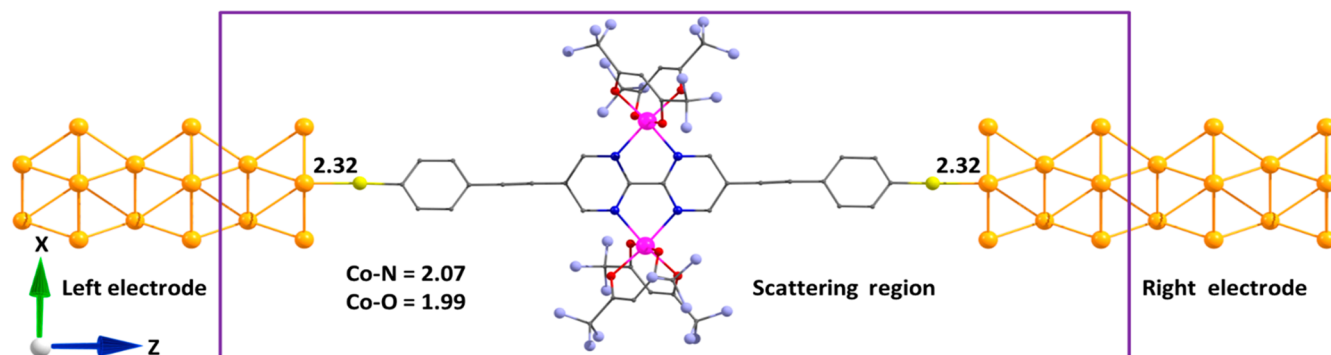


**Figure 2.** Molecular junction device of  $1I_{hshs}$ . Color code: pink, Co; yellow S; deep yellow, Au; light blue, F; red, O; blue, N; gray, C. Hydrogen atoms have been omitted for clarity. Here, the Z-direction is the transport direction, and the Fermi energy is set to zero. Bond lengths (Å) of Au–S, Co–N, and Co–O are shown.

that the community has been attempting to solve for a long time. While **1** has been shown to have an  $S = 0$  ground state arising from antiferromagnetic coupling, an excited pseudo triplet exchange-coupled state was accessible via a bias-voltage.<sup>27</sup>

Here, the goal of the work is to study the magnetic and quantum transport properties of a molecular junction device constructed by tethering complex **1** to the gold nanowires (leads) with an aim to answer the following intriguing questions: (i) Do the spin-state and spin-coupled state of Co(II) alter upon tethering at the interface? (ii) What is the role of exchange interactions and ligand-field induced spin-states (high-spin vs low-spin) in modulating the transport characteristics? (iii) Is the observation of the negative differential resistance (NDR) effect, spin-state dependent? And what is the origin of the NDR observed? (iv) Is it possible to improve both NDR performance as well as spin-filtering efficiency via exchange-coupling or ligand field modulation?

## COMPUTATIONAL DETAILS

A periodic DFT/PBE optimization of complex **1** (see Figure 1(a)) and a molecular junction device was performed using Geodecker-Tetter-Hutter (GTH) pseudopotential, double- $\zeta$ -valence-polarized (DZVP) basis sets for all atoms and the Gaussian augmented plane wave (GAPW) method as implemented in the CP2K-6.1.0 suite.<sup>28,29</sup> The employed pseudopotential was expected to address the relativistic effects of the heavier elements.<sup>30</sup> Perdew–Burke–Ernzerhof (PBE) generalized gradient approximation (GGA) for the exchange-correlation functional and an energy cutoff of 400 eV and convergence cutoff of  $10^{-4}$  eV/Å were used.<sup>31</sup> To construct a molecular junction device, we used gold Au (111) nanowires as left (L) and right (R) electrodes and a buffer region to avoid close contact of electrodes with the molecular device.<sup>32,33</sup> The optimization of molecular junction devices was carried out without any constraints on the atomic positions of the gold atoms. The  $-\text{COCH}_3$  group attached to sulfur in **1** is modified to a sulfur neutral (radical) atom to make stable interactions with an odd number of Au interfaces, enabling strong gold and sulfur radical antiferromagnetic coupling, which is extremely strong and has therefore been considered as an overall singlet state.<sup>34</sup> The central scattering region consists of a few gold atoms and complex **1** (see Figure 2). The Au–S bond distance is found to be 2.32 Å. The magnetic exchange coupling constant ( $J$ ) in complex **1** and at the interface between different spin states was computed with B3LYP/def2TZVP methodology using Noodleman's broken symmetry approach in the Gaussian 09 suite.<sup>35–37</sup>

To compute the zero-field splitting (ZFS) parameters (D, E) and magnetic anisotropy of Co(II) metal centers, the ORCA-4.0.1 suite of programs was used.<sup>38</sup> The complete active space self-consistent field-quasi degenerate perturbation theory-effective Hamiltonian approach

(CASSCF-QDPT-EHA) followed by *ab initio* ligand field theory (AILFT) has been performed.<sup>39–41</sup> The NEVPT2 (n-electron valence second-order perturbation theory) calculations were also performed on the top of the CASSCF wave function to account for the dynamic correlation.<sup>42–44</sup> To account for the scalar relativistic effect, a second-order Douglas Kroll Hess (DKH) Hamiltonian was used. The DKH-contracted version of basis sets like DKH-def2-TZVP (triple- $\zeta$  valence polarized) for Co and S and DKH-def2-TZVP(-f) for N and DKH-def2-SVP for the rest of the atoms was used during the calculations. The CASSCF-NEVPT2 energies were calculated by considering 10 quartet roots and 40 doublet roots. An active space of CAS(7, 5) was used to calculate the ZFS parameters of each Co(II) center, and the corresponding orbitals that are employed for this calculations are shown in the SI. The quantum coherent transport properties were calculated using DFT combined with the NEGF formalism implemented in the Transiesta code.<sup>45–48</sup> We used the PBE exchange-correlation functional for our calculations.<sup>49</sup> Troullier-Matins norm-conserved pseudopotentials were applied to define the interaction between the valence and core electrons.<sup>50</sup> We used a single- $\zeta$ -polarized (SZP) basis set and one electron pseudopotential for the Au atoms, while the double- $\zeta$ -polarized (DZP) basis set was used for all other atoms.<sup>49</sup> A mesh cutoff of 150 Ry was used to describe the grid's density, and  $\Gamma$ -points for Brillouin zone sampling were used for both real and reciprocal space grids. To compute the spin-polarized current through a molecular junction device, a finite bias voltage was applied across the leads ranging from 0.0 to 1.0 V (in steps of 0.1 V). We computed the zero-bias transmission spectra [ $T_\sigma(E, V)$  at an applied bias of  $V = 0$ ] using eq 1:

$$T_\sigma(E, V) = \text{Tr}[\Gamma_L G_\sigma \Gamma_R G_\sigma^\dagger] \quad (1)$$

Here,  $\sigma$  stands for the spin-up and spin-down channels ( $\sigma = \uparrow/\downarrow$ ).  $G_\sigma$  is the retarded Green's function of the scattering region, and  $\Gamma_{L/R}$  is the coupling matrix between the scattering region and the left/right electrode. The spin-resolved current (under externally applied biases) through the molecular junction device is calculated using the Landauer-Büttiker formula<sup>33,51</sup> as shown in eq 2

$$I_\sigma(V) = \frac{e}{h} \int T_\sigma(E, V) [f(E - \mu_L) - f(E - \mu_R)] dE \quad (2)$$

where  $f(E - \mu_{L/R})$  is the Fermi function, while  $\mu_{L/R}$  stands for the chemical potential of the left/right electrode. The SFE at a given bias voltage is defined as

$$\text{SFE} = \frac{|I_\alpha(V) - I_\beta(V)|}{|I_\alpha(V) + I_\beta(V)|} \quad (3)$$

and the SFE at zero bias voltage is calculated as

$$\text{SFE}(V = 0) = \frac{|T_\alpha(E) - T_\beta(E)|}{|T_\alpha(E) + T_\beta(E)|} \quad (4)$$

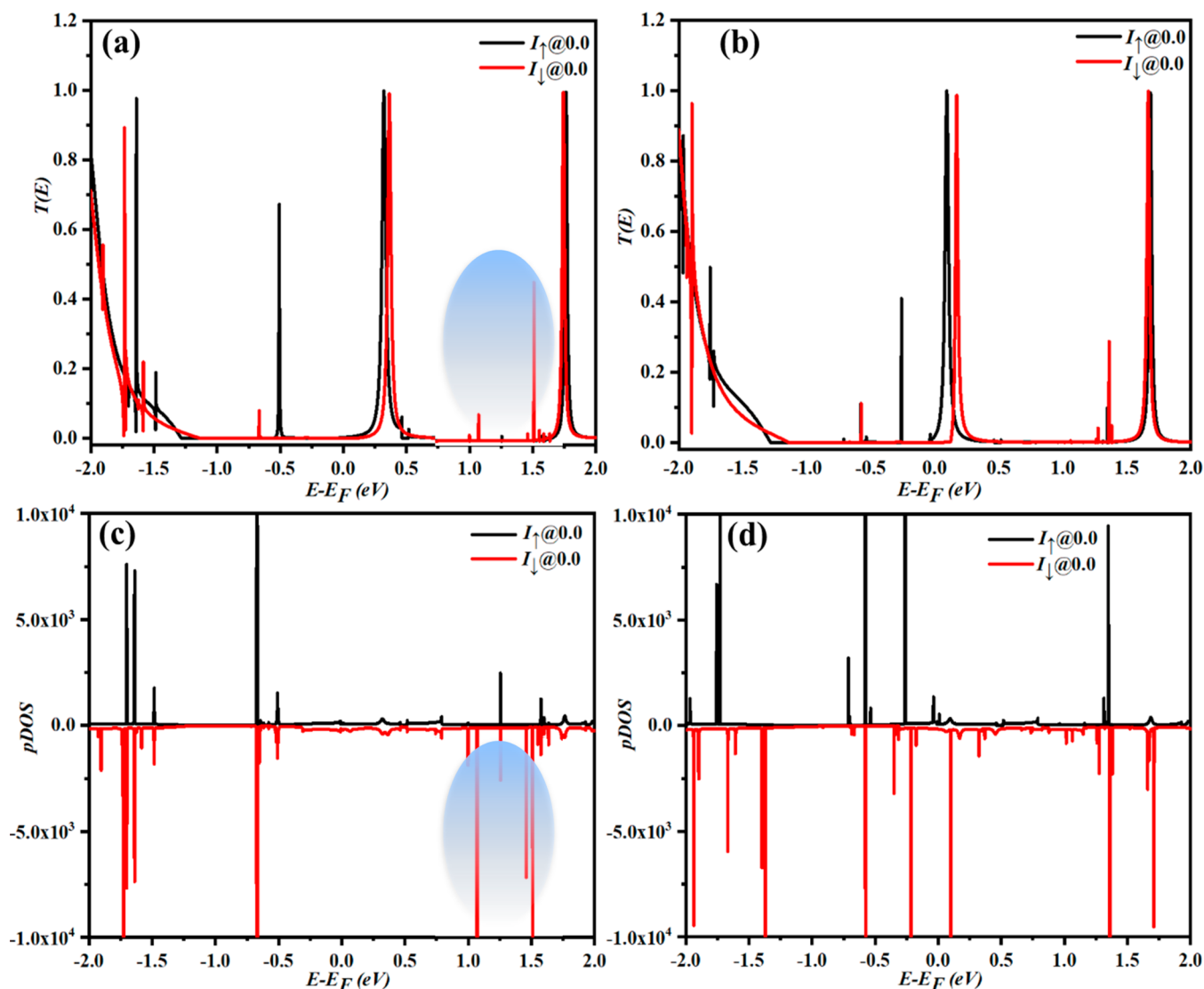


**Figure 3.** Spin-resolved  $T(E)$  (upper panel) and  $pDOS$  (down panel) of  $^1I_{hshs}$  (a, c) at zero-bias voltage and  $^3I_{lsls}$  (b, d) at zero-bias voltage. Black and red colors correspond to the  $\alpha$  and  $\beta$  spin channel contributions, respectively. The Fermi energy ( $E_F$ ) is set to zero. The blue elliptical highlights indicate difference in polarization.

where  $T_\alpha$  and  $T_\beta$  are transmission coefficients for  $\alpha$  and  $\beta$  states at the Fermi energy level, respectively.

The role of the Au–S bond length on the transmission spectra is found to be insignificant for the transport characteristics in the earlier work reported by Ruiz and co-workers, and therefore, here, we have kept the Au–S bond length to an optimized value, which is similar to the recommended value.<sup>18</sup>

We have employed the terminology  $^M I_{ss}$  to denote various spin states chosen, and here, superscript  $M$  denotes the overall spin-multiplicity of the state. The subscript “ss” denotes individual spin-state (hs or ls) on Co(1) and Co(2) centers, respectively.

## RESULTS AND DISCUSSION

**Spin-State Energetics and Estimation of Magnetic Exchange.** The X-ray structure of complex **1** was reported earlier,<sup>27</sup> and here, each Co(II) center in the distorted octahedral geometry with four oxygen atoms of the hexafluoroacetylacetonato and two nitrogen atoms of the bipyrimidine ligand coordinated to the metal center. A strong exchange coupling between the two Co(II) centers is expected as bipyrimidine is bridging the two Co(II) centers offering a superexchange pathway. To begin with, the X-ray structure of

complex **1** was optimized using the DFT methods for spin-coupled states ( $S_T$ ) of  $S_T = 0, 1, 2,$  and  $3$  (see Figure S1(a) and Table S1 in the SI). Here, two Co(II) centers are assumed to be in either high-spin ( $S = 3/2$ ) or low-spin ( $S = 1/2$ ) or in-between, with one Co(II) center being in the  $S = 3/2$  state and the other in the  $S = 1/2$  state. These individual spin-states could couple ferromagnetically or antiferromagnetically, leading to  $S_T = 3$  or  $0$  ( $^7I_{hshs}$  and  $^1I_{hshs}$ ),  $1$  or  $0$  ( $^3I_{lsls}$  and  $^1I_{lsls}$ ), and  $2$  or  $1$  ( $^5I_{hshs}$  and  $^3I_{hshs}$ ) depending on the nature of the spin-state at the Co(II) centers. Among these spin-states, we have successfully optimized the geometries of  $^1I_{hshs}$ ,  $^7I_{hshs}$ ,  $^1I_{lsls}$ , and  $^3I_{lsls}$  states. Here,  $^1I_{hshs}$  was found to be the ground state, with  $^7I_{hshs}$ ,  $^1I_{lsls}$ , and  $^3I_{lsls}$  states lying higher at 0.3, 112.0, and 112.3 kJ/mol, respectively. The ground state Co(II) centers were found to have  $(d_{xz})^\uparrow(d_{yz})^\uparrow(d_{xy})^\uparrow(d_{x^2-y^2})^\uparrow(d_z)^\uparrow$  configuration with the spin density of 2.72 on each Co(II) center with small positive spin densities on the coordinated N and O atoms ( $\sim 0.04$ ) (see Figure S1(c, d) in the SI). To compute the magnetic exchange coupling constant ( $J$ ), we have used the Hamiltonian of  $\hat{H} = -2J\hat{S}_1\hat{S}_2$  and broken symmetry

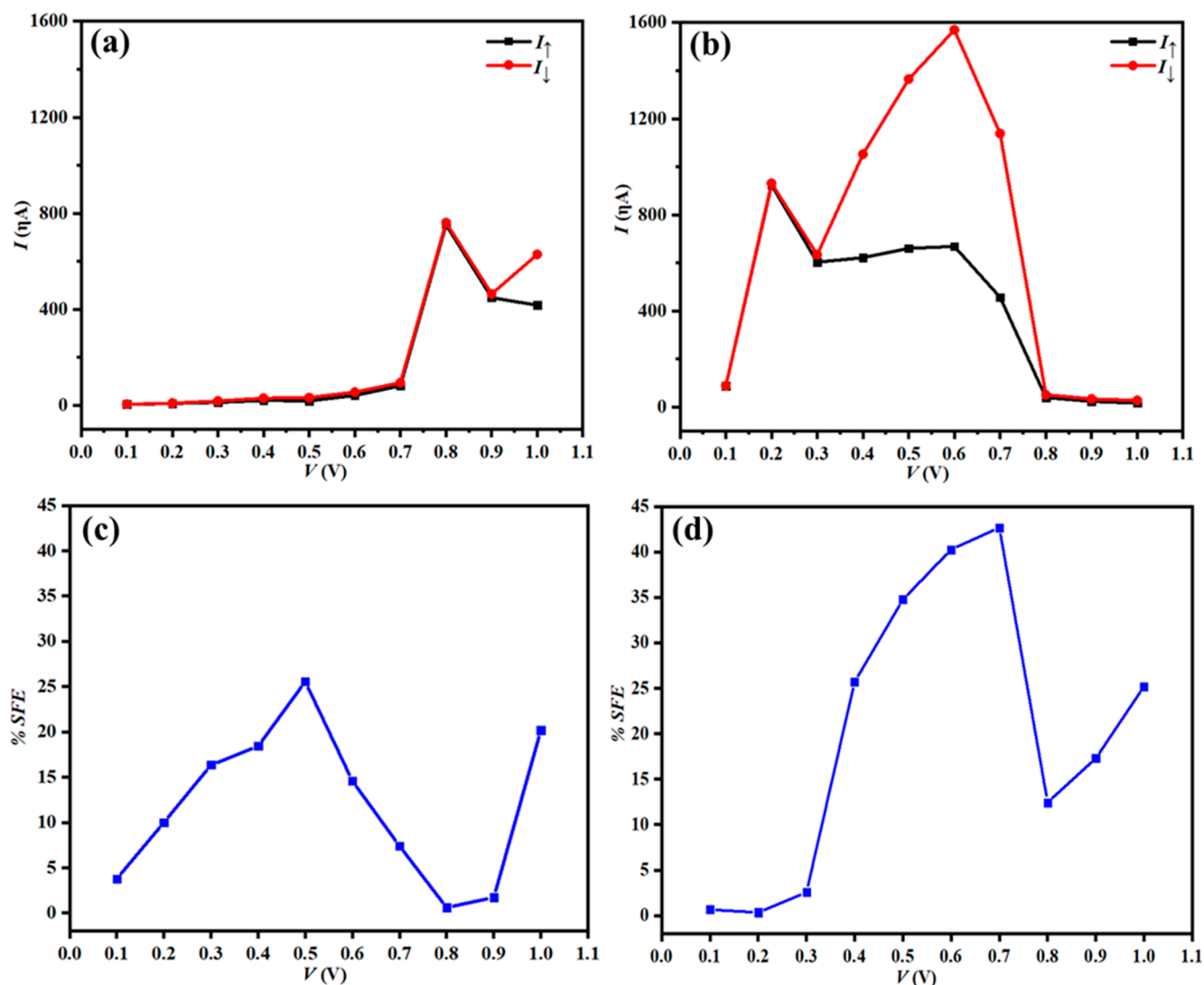


**Figure 4.** (a, c) represent the  $I$ - $V$  and  $SFE$  plots of the  $^1\mathbf{I}_{\text{hshs}}$  state, while (b, d) show the  $I$ - $V$  and  $SFE$  plots of the  $^3\mathbf{I}_{\text{lsls}}$  state, respectively.

approach (here,  $S_1$  and  $S_2$  are spin states of metal centers). DFT calculations using the B3LYP functional on the optimized geometry of **1** yield antiferromagnetic coupling with the  $J$  value of  $-2.1 \text{ cm}^{-1}$  between two Co(II) centers, which agrees with the reported value of  $-0.39 \text{ cm}^{-1}$  computed by Wagner et al., where magnetic exchange was computed using the CASSCF-SOCI method (Figure S1(b) in the SI).<sup>27</sup> The weak antiferromagnetic coupling results from a strong  $\langle 3d_{x^2-y^2} | 3d_{x^2-y^2} \rangle$  overlap of Co(II) centers via the bridging ligand, and this contributes to the antiferromagnetic part of the exchange and orthogonality of  $d_z^2$  and  $d_{xy}$  singly occupied molecular orbitals (SOMOs) contributing to the ferromagnetic part of the exchange (see Table S2 in the SI). However, at the interface ( $\text{Au}_7\text{-}^1\mathbf{I}_{\text{hshs}}\text{-Au}_7$ ), the strength of the antiferromagnetic exchange becomes even stronger with the estimated  $J$  value of  $-38 \text{ cm}^{-1}$ . It is found that the angles ( $\angle\text{Co1-N-C}$ ,  $\angle\text{N-C-N}$ , and  $\angle\text{C-N-Co2}$ , see Figure S14) connecting two cobalt centers at the interface become more linear and therefore impart stronger overlap between the  $\langle 3d_{x^2-y^2} | 3d_{x^2-y^2} \rangle$  and  $\langle d_{xy} | d_{xy} \rangle$  orbitals (see Table S2 in the SI) contributing to the stronger antiferromagnetic exchange between the Co metal centers. The magnetic anisotropy is expected to be significant as the Co(II) centers have a distorted octahedral geometry.

**Zero Field Splitting of Co(II) Centers.** To assess and analyze the zero-field splitting (ZFS) parameters, we have performed *ab initio* CASSCF/NEVPT2 calculations on a fictitious model where one of the Co(II) centers was replaced by a Zn(II) ion. This yielded  $D = +39 \text{ cm}^{-1}$  with an  $E/D$  of 0.28 (see Table S3 in the SI). The *ab initio* ligand field theory (AILFT) computed d-orbitals are shown in Figure 1, and this reveals that there are three prominent contributions to the single-ion  $D$  value, i.e.,  $d_{xz}$  to  $d_{xy}$  transition ( $+24 \text{ cm}^{-1}$ ),  $d_{yz}$  to  $d_{xy}$  transition ( $+16 \text{ cm}^{-1}$ ), and  $d_{xy}$  to  $d_{x^2-y^2}$  transition ( $-11 \text{ cm}^{-1}$ ). A closer look at the ground state configuration computed reveals contributions from various configurations suggesting multideterminant character for the ground state (see Table S4 in the SI). Each Co(II) center shows magnetic anisotropy with  $g_x$ ,  $g_y$ , and  $g_z$  of 2.074, 2.334, and 2.574, respectively (see Figure S2(a, b) for  $g$  and  $D$  directions). The computed  $+D$  value at the CASSCF-SOCI level ( $54 \text{ cm}^{-1}$ , see Table S4 in the SI) for **1** is also similar to the value computed by Wagner et al. ( $75 \text{ cm}^{-1}$ ) providing confidence with the computational methodology chosen.<sup>27</sup> The computed electronic Hamiltonian and positive ZFS for single-ion anisotropy are also preserved at the interface (i.e., optimized geometry at the interface) with an estimated  $D$  value of  $+30 \text{ cm}^{-1}$ , with a

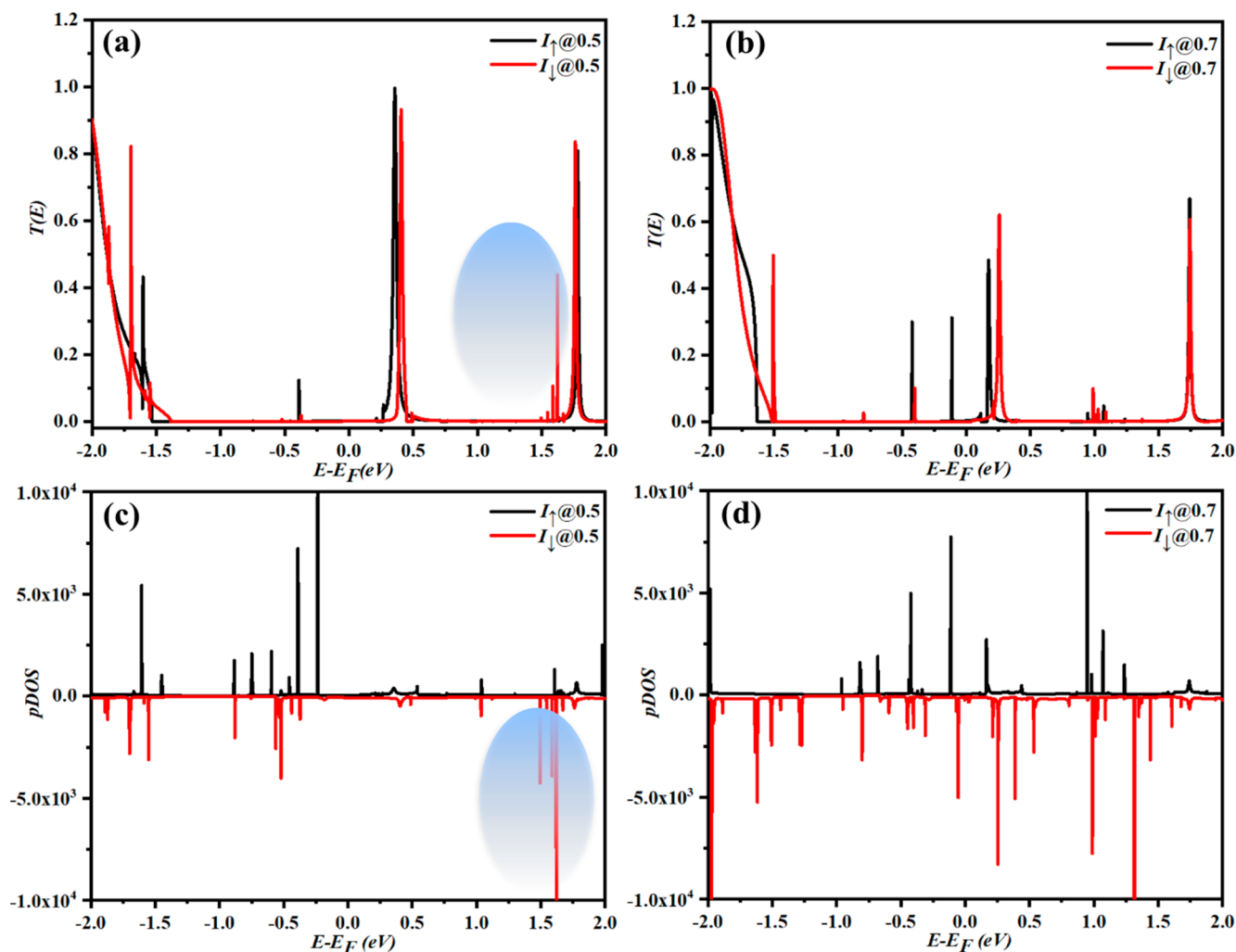


**Figure 5.** Bias-dependent spin-resolved  $T(E)$  (upper panel) and  $pDOS$  (down panel) of  $^1\mathbf{I}_{hshs}$  (a, c) at a 0.5 V bias voltage and  $^3\mathbf{I}_{lshs}$  (b, d) at 0.7 V. Black and red colors correspond to the  $\alpha$  and  $\beta$  spin channel contributions, respectively. The blue elliptical highlights indicate difference in polarization.

slight reduction compared to the X-ray geometry (see Table S3). The three contributions that contribute to the single-ion D value are the  $d_{xz}$  to  $d_{xy}$  transition ( $+20\text{ cm}^{-1}$ ),  $d_{yz}$  to  $d_{xy}$  transition ( $+15\text{ cm}^{-1}$ ), and  $d_{xy}$  to  $d_{x^2-y^2}$  transition ( $-10\text{ cm}^{-1}$ ) (see Figure S2(c)). The slight decrease in the value of D is noted due to an increase in the Co–N/O bond length by  $0.097\text{ \AA}$ , which causes weaker ZFS.

**Coherent Quantum Transport of Complex 1.** To investigate the quantum transport properties of the modeled device (see Figure 2), a finite bias voltage is applied across the molecular junction device ranging from 0.0 to 1.0 V. There is no flow of current through the device in the absence of external bias voltage (at  $V = 0$ ) as the left and right electrodes are in equilibrium having the same chemical potential ( $\mu_L = \mu_R$ ). When a bias voltage is applied (at  $V \neq 0$ ), the chemical potential of the left electrode ( $\mu_L$ ) is increased, and the chemical potential of the right electrode ( $\mu_R$ ) is expected to decrease to the same extent. Therefore, a potential difference (bias window) is set between the electrodes, and the flow of a spin-polarized current is noted across the device. To analyze the spin-resolved current, we investigate the zero-bias transmission spectra,  $T(E)$  and corresponding projected density of states ( $pDOS$ ) (see Figures 3(a–d), S3 in the SI). Although

several spin-coupled states are possible at the interface and at a certain bias voltage various spin-states could be present as a mixed state at the junction, coherent transport properties were calculated on the three low-lying spin-coupled states  $^1\mathbf{I}_{hshs}$ ,  $^3\mathbf{I}_{lshs}$ , and  $^7\mathbf{I}_{hshs}$  as other spin states are very high in energy ( $>150\text{ kJ/mol}$ ).

**Coherent Transport across the Singlet State Arising from the Antiferromagnetic Interaction of  $S = 3/2$  States ( $^1\mathbf{I}_{hshs}$ ).** For a single-molecule junction device with  $^1\mathbf{I}_{hshs}$  geometry (singlet state antiferromagnetic coupled due to  $S = 3/2$  on each Co(II) center), the transmission spectra for spin-up and spin-down channels reveal broad peaks around the Fermi energy (see Figure 3(a)). The  $pDOS$  of  $\beta$ -states lies around 1.1 and  $-0.7\text{ eV}$  in the conduction and valence bands, respectively (see Figure 3(c)). While  $\alpha$ -states are far from Fermi energy in the conduction band and the intensity of  $\beta$ -states peak is significant, a one  $\alpha$ -state peak with significant intensity is found in the valence band at around  $-0.7\text{ eV}$  (see Figure 3(a, c)). As the  $pDOS$  ( $\alpha$  and  $\beta$ ) with significant intensity is not found near the Fermi energy level, the current flow through the device is expected to be very low. The  $I$ – $V$  plot (Figure 4(a)) suggests that the current flowing through the molecular junction is of the order of a few nanoamperes ( $\eta\text{A}$ ) ( $0$ – $10\text{ }\eta\text{A}$ ) at an applied

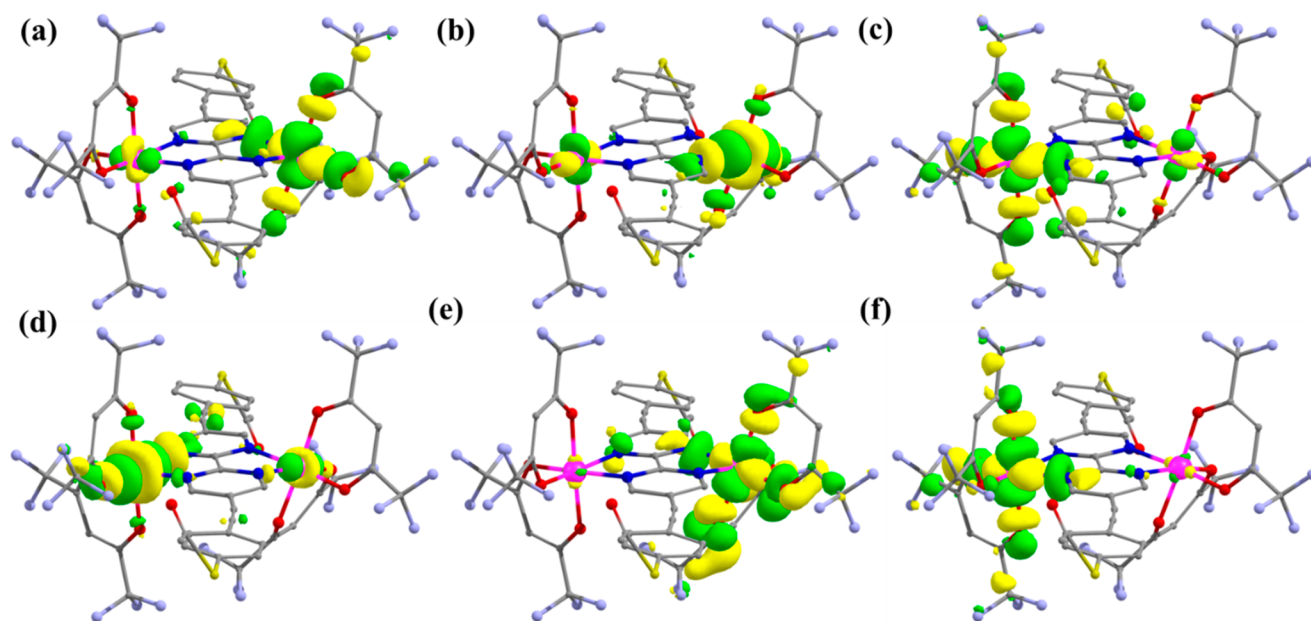


**Figure 6.** For  ${}^3\mathbf{1}_{\text{sls}}$  (a–d) show empty  $\beta$  d-orbitals ( $e_g$ ) lying on Co1 and Co2 metal centers, while (e, f) orbitals show  $\alpha$  empty orbitals. These orbitals are closer to the Fermi level and make large contributions to the transmission.

bias of 0.7 V. A similar result has been demonstrated by Weber and co-workers experimentally, where the current order of a few  $\eta\text{A}$  (0–10  $\eta\text{A}$ ) was found to flow through a single-molecule junction device (Au– ${}^1\mathbf{I}_{\text{hshs}}$ –Au) until the applied bias voltage of 0.7 V.<sup>27</sup> An increase in the magnitude of the current is noted at 0.8 V applied bias followed by a drop at 0.9 V applied bias which exhibits the characteristics of a NDR, see the NDR section and has also been observed experimentally at high bias voltage.<sup>27</sup> The percentage of SFE is calculated using eq 3, and an SFE of 24% was found at an applied bias of 0.5 V. To comprehend the mechanism of a high SFE estimated, we plot the  $p\text{DOS}$  and  $T(E)$  (see Figure 5(a, b)) at a 0.5 V bias. Analysis of the  $p\text{DOS}$  plot reveals that there are more  $\beta$ -states available near the Fermi energy (in both positive and negative energy regions); this gives the polarization to the current, and the spin-down current ( $I_{\downarrow}$ ) was found to be a major transport channel (carrier) at all of the applied bias voltages. At 1.5 eV away from the Fermi energy in the conduction band, the available  $\beta$ -states have significant  $T(E)$  around 0.45, which causes the  $\beta$ -polarized current to be a major channel (see the highlighted area in Figures 3(a, c) and 5(a, c)). The polarization in the current could also arise due to a mixing of very close (0.3  $\text{kJ mol}^{-1}$  higher in energy) excited state  ${}^7\mathbf{1}_{\text{hshs}}$  in the presence of an applied bias. The spin-down channel is dominant (transmitting more electrons) under the applied bias, leading to an increase in the  $I_{\downarrow}$  compared to the spin-up current ( $I_{\uparrow}$ ). Furthermore, a sudden rise in the current is noted when the bias voltage is increased from 0.7 to 0.8 V. This could be due to bias-dependent transmission, and  $p\text{DOS}$  analysis shows the emergence of a larger number of electronic states close to the Fermi level. At a 0.7 V bias, there are three  $\beta$ -peaks with no  $\alpha$ -peak in the bias window (see the  $-0.35$  to  $0.35$  V energy window in Figure S12). However, at a 0.8 V bias, there are four  $\beta$ -peaks and two  $\alpha$ -peaks with significant intensity ( $-0.4$  to  $0.4$  V, Figure S10), which leads to a shift in transmission resonance peaks close to the Fermi level with relatively high transmission intensity (see Figures S10 and S12). A significant increase in both intensity and number of  $\alpha$

and  $\beta$  peaks from the 0.7 to 0.8 V bias window, along with an increase in the  $T(E)$  value, results in the observation of enhancement in the current. At a 1.0 V bias, the number of  $p\text{DOS}$  in the bias window of  $[-0.5, 0.5]$  eV for  $I_{\uparrow}$  and  $I_{\downarrow}$  channels differs significantly. In the bias window, there are only two  $\alpha$ -peaks with significant intensity (Figure S10(a)), while five  $\beta$ -peaks with significant intensity (Figure S10(b)) are available for the transport; this results in the spin polarization.

**Coherent Transport across the Triplet State Arising from the Ferromagnetic Interaction of  $S = 1/2$  States ( ${}^3\mathbf{1}_{\text{sls}}$ ).** In the  ${}^3\mathbf{1}_{\text{sls}}$  state, the  $p\text{DOS}$  for  $\beta$ -states shows a higher number of electronic states than  $\alpha$ -states close to the Fermi level (see Figure 3(b, d)). This is mainly a result of the presence of empty  $\beta$   $t_{2g}$  and  $e_g$  orbitals near the Fermi energy at around 1.4 eV. The electron in the  $e_g$  orbitals and the rest of the  $t_{2g}$  electrons are found near 0.2, 1.3, and 1.5 eV, respectively, in the conduction band. It is interesting to note that transmission spectra, as well as  $p\text{DOS}$  figures, show two resonance peaks/states at around 1.65 and 1.66 eV for  $\beta$ -states and one resonance peak at around 1.68 eV for  $\beta$ -states (see Figure 3(b, d)). However, we see that these strong resonance peaks are being supported by the  $p\text{DOS}$  of  $\beta$ -states with high intensity, but for  $\alpha$ -states, the intensity is relatively smaller. A result of the  $p\text{DOS}$  and  $T(E)$  peaks of the  ${}^3\mathbf{1}_{\text{sls}}$  state suggests the possibility of spin-filtering and polarized current through the proposed molecular junction. To compute the extent of polarized conductance, we have performed several bias-dependent transport calculations in the presence of bias voltage ranging from 0.1 to 1.0 V (in steps of 0.1 V). It is ecstatic to see that  $I_{\uparrow}$  and  $I_{\downarrow}$  flowing through the molecular-junction are almost the same up to 0.3 V for  ${}^3\mathbf{1}_{\text{sls}}$  states/geometries (see Figure 4(b)) and zero SFE. As the bias is further increased, the flow of the current is also increased. However,  $I_{\downarrow}$  becomes a major channel of transport, and a finite SFE is achieved later at large biases. On the other hand, both  $I_{\uparrow}$  and  $I_{\downarrow}$  show clearly an NDR with an onset bias of 0.3 V and after 0.6 V applied biases. It is found that (i)  $I_{\downarrow}$  is always a major channel of transport (see Figure 4(b)), and (ii) while

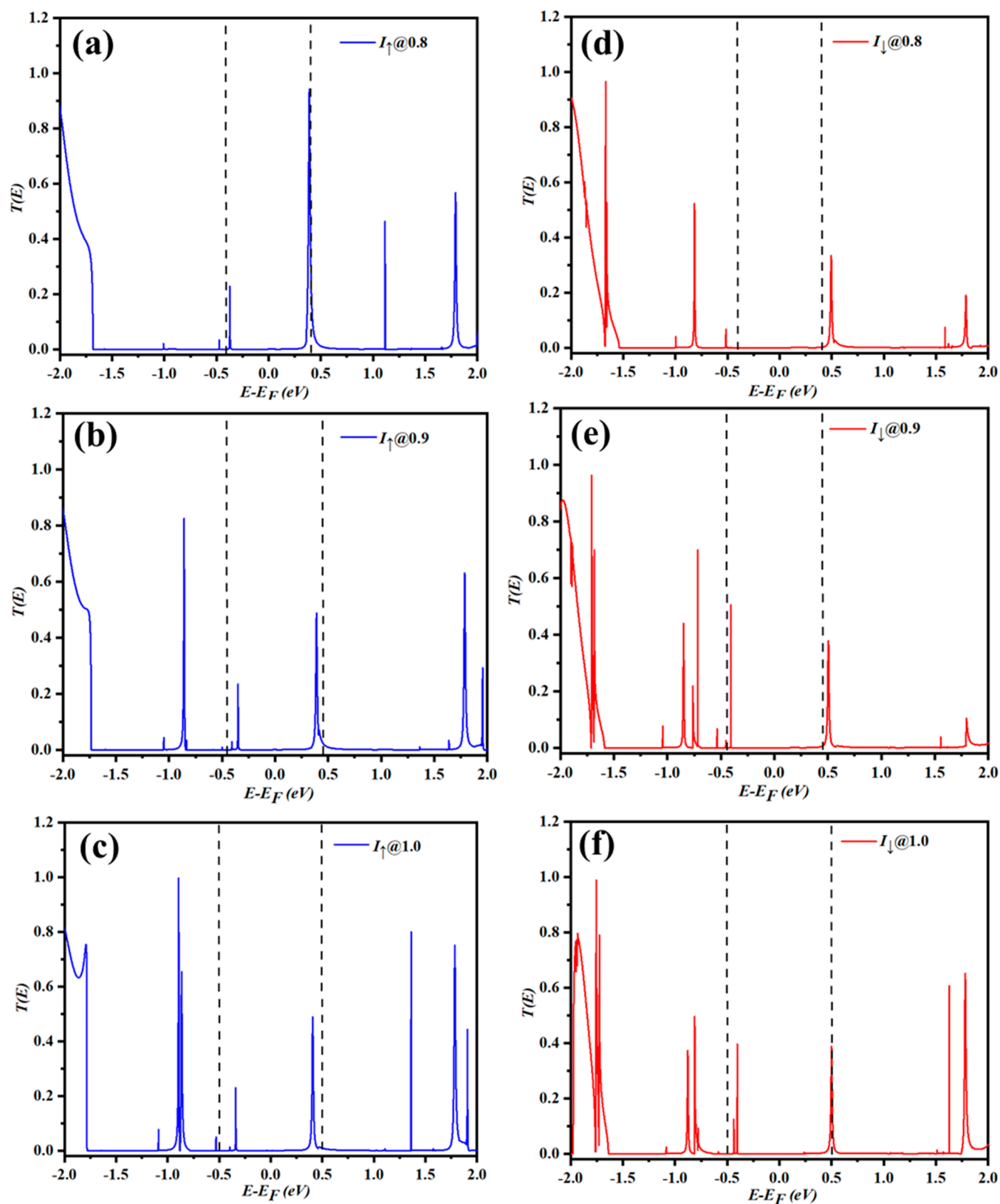


**Figure 7.** Bias-dependent spin polarized  $T(E)$  spectra of  $\alpha$ - and  $\beta$ -states of  $^1I_{\text{hshs}}$  at 0.8 (a, d), 0.9 (b, e), and 1.0 V (c, f), respectively.

the order of the magnitude of the current is around  $\eta\text{A}$ , a maximum current is observed at around a 0.6 bias voltage in  $^3I_{\text{ls}}$  spin states (see Figure 4(b)). (iii) A spin filtering of the current is noted at all applied bias voltages, and a maximum SFE of 44% is found in  $^3I_{\text{ls}}$  spin states at an applied bias of 0.7

V (see Figure 4(d)). To shed light on the high SFE observed in the  $^3I_{\text{ls}}$  spin state, we further plotted the spectra of  $T(E)$  and  $p\text{DOS}$  as shown in Figure 5(b, d). Figure 5(b) suggests that near the Fermi energy, four  $\beta$ -empty states were present in the conduction band (corresponding to the  $e_g$  orbitals of the two

Co(II) centers, see Figure 6(a-d)) and one  $\alpha$  occupied state in the valence band, which corresponds to the occupation of a single electron in the  $e_g$  orbitals, and the rest of the  $t_{2g}$  electrons are found near  $-0.4$  eV below the Fermi level. Further, there is one occupied and one unoccupied  $\alpha$  state (corresponding to the  $e_g$  orbitals, see Figure 6(e, f)) present in valence and conduction bands, respectively. Also, the transmission coefficient for  $\beta$  states is significantly higher than that for  $\alpha$  states. In the  $^3\mathbf{1}_{\text{ls}}$  spin state, each  $\text{Co}^{\text{II}}$  center possesses a  $t_{2g}^6 e_g^1$  electronic configuration; a weak antiferromagnetic interaction is computed between two  $S = 1/2$  states, and the computed  $J$  here corresponds to  $-24 \text{ cm}^{-1}$ . This electronic configuration results in a 44% *SFE* for this state. We carefully compared the  $I$ - $V$  characteristics (Figure 4(b)) of these two states, i.e.,  $^1\mathbf{1}_{\text{hshs}}$  and  $^3\mathbf{1}_{\text{ls}}$  states; it is clear that the observed current in  $^3\mathbf{1}_{\text{ls}}$  is larger for both  $I_{\downarrow}$  and  $I_{\uparrow}$  states, but a tremendous increase is seen for  $I_{\downarrow}$ . This is essentially due to the additional two  $e_g$   $\alpha$ -holes available for transport compared to the other states where only two  $t_{2g}$   $\beta$ -holes are available for transport. As shown earlier, the conductance is more efficient with the  $e_g$  orbitals than with nonbonding  $t_{2g}$  orbitals, rationalizing the observed difference state; each  $\text{Co}^{\text{II}}$  center possesses a  $t_{2g}^6 e_g^1$  electronic configuration, and a weak antiferromagnetic interaction is computed here.<sup>20</sup>

**Coherent Transport across the Septet State Arising from the Ferromagnetic Interaction of  $S = 3/2$  States ( $^7\mathbf{1}_{\text{hshs}}$ ).** In the  $^7\mathbf{1}_{\text{hshs}}$  state, each Co(II) center has an electronic configuration of  $t_{2g}^5 e_g^2$  and is ferromagnetically coupled, leading to an overall  $S = 3$  spin ground state. Zero-bias  $T(E)$  (Figure S3(a)) suggests that  $T(E)$  for  $\alpha$  and  $\beta$  states near the Fermi energy is equivalent. Similarly, the  $p$ DOS suggests that the equivalent number of  $\alpha$  and  $\beta$  states is available near the Fermi energy. However, at around 1.5 eV near the Fermi energy, the DOS of  $\beta$  states is significant compared to  $\alpha$  states, suggesting the possibility of observing a polarized current at an applied bias. When a bias voltage is applied across the molecular junction device, a maximum current of around 760  $\eta\text{A}$  at a 0.8 V applied bias is obtained (Figure S3(e)). A sudden increase in the current is noted when the bias voltage is increased from 0.7 to 0.8 V due to the availability of larger DOS at the Fermi energy with high  $T(E)$  values (see Figures S5 and S12). At 0.9 V bias, a slight decrease in current is obtained, suggesting NDR behavior (see the NDR section). Similar to other spin states, in  $^7\mathbf{1}_{\text{hshs}}$ , a significant spin-polarized current is noted where  $I_{\downarrow}$  was found to be a major transport channel. A maximum *SFE* of 25% was found at a 0.5 applied bias voltage. To compute the mechanism for  $I_{\downarrow}$  as a major carrier, spectra of  $T(E)$  and  $p$ DOS were plotted at a 0.5 bias voltage (see Figure S3(d)). It is found that in the conduction band at around 1.1 and 1.6 eV to the Fermi level, a total of three extra  $\beta$ -states are available, and the corresponding  $T(E)$  is significant ( $T(E) = 0.4$ , Figure S3(b)). These  $\beta$ -states are due to the presence of three  $\beta$ -orbitals (one  $t_{2g}$  and two  $e_g$ , see Figure S4(a-f)) to each  $\text{Co}^{\text{II}}$  ( $t_{2g}^5 e_g^2$ ) metal center, and hence, the  $\beta$ -current is found as a major transport channel.

**Negative Differential Resistance.** Observation of NDR in molecular electronics has great interest due to its potential applications in switches, energy harvesting, sensors, and quantum computing due to its unique bistability with different current levels.<sup>52-59</sup> Several proposed mechanisms have been used to describe the NDR effect, such as molecule-electrode coupling,<sup>60-62</sup> misalignment of molecular orbitals,<sup>63-65</sup> sharp DOS of the electrode,<sup>66</sup> quantum interference,<sup>67,68</sup> etc. The

NDR effect has been reported in metal-doped systems,<sup>69</sup>  $\pi$ -conjugated systems,<sup>70</sup> and organic/inorganic molecules<sup>71,72</sup> connected to electrodes. In the molecule studied here, an NDR phenomenon is also observed at some applied bias in different magnetic states. For example,  $I_{\uparrow}$  of  $^1\mathbf{1}_{\text{hshs}}$  and  $^7\mathbf{1}_{\text{hshs}}$  states shows an NDR effect at a bias voltage of 0.9 V, and  $I_{\downarrow}$  shows NDR in the region of [0.9, 1.0] V (see Figures 4(a) and S3). Similarly, in  $^3\mathbf{1}_{\text{ls}}$ , both  $I_{\uparrow}$  as well as  $I_{\downarrow}$  show an NDR effect at an applied bias of 0.3 V and in the region of [0.6, 1.0] V (see Figure 4(b)). Experimental  $I$ - $V$  features also exhibit an NDR effect at  $\sim 0.85$  V, offering confidence in the computed data. We analyze the bias-dependent transmission to understand the physics behind the NDR effect observed for these systems. To compute the origin of NDR at 0.9 V in the  $^1\mathbf{1}_{\text{hshs}}$  state, we plot the bias-dependent  $T(E)$  spectra at 0.8, 0.9, and 1.0 V, respectively (see Figure 7). The  $T(E)$  spectra for  $I_{\uparrow}$  at 0.8 V bias show that there are two transmission peaks in the bias window of  $[-0.4, 0.4]$  V with  $T(E) = 0.04$  and 0.95. When a bias voltage of 0.9 V is applied, no additional peak is observed in the bias window of  $[-0.45, 0.45]$  V (see Figure 7(b)); however, the coefficient of two transmission peaks becomes  $T(E) = 0.05$  and 0.50 (decreased from 0.95 to 0.50), and hence, an overall decrease in the current is expected as observed. Again at a 1.0 V bias voltage applied, the  $T(E)$  coefficient for one of the peaks decreases further to 0.45, and no new transmission peak appears in the bias window of  $[-0.5, 0.5]$  V (see Figure 7(c)) leading to a further decrease in the current and hence observation of NDR. Moreover, we observed that those two peaks are moving close to the Fermi energy as we increase the applied bias from 0.8 to 1.0 V. Previously, such behavior has been observed in graphene molecular devices.<sup>73</sup> Similar to  $I_{\uparrow}$ ,  $T(E)$  spectra were also plotted for  $I_{\downarrow}$  (see Figure 7). It is observed that there is no peak with a significant transmission coefficient in the bias window of  $[-0.4, 0.4]$  V at 0.8 bias and also at 0.9 V ( $[-0.45, 0.45]$  V window). However, at an applied bias of 1.0 V, there are two peaks with  $T(E) = 0.09$  and 0.40 present in the bias window of  $[-1.0, 1.0]$  V. Hence moving from 0.8 to 0.9 V applied bias, a decrease in the current is noted followed by an increase in the current at 1.0 V bias. The  $p$ DOS state reveals (see Figure S10) that increasing the bias voltage from 0.8 to 1.0 V split the orbitals that lie within the bias window, and these orbitals correspond to the empty  $t_{2g}$  and  $e_g$  orbitals of the Co(II) center. Increasing the voltage is found to generate a larger energy gap (0.05–0.1 eV) between these two orbitals that might be leading to a relatively weaker coupling with the electrodes, and hence, a drop in the  $T(E)$  leads the NDR effect in this device. However, since we do not have conclusive evidence on this phenomenon except a decrease in the transmission function and drop in the current at certain applied biases, we suspect that some other factors are also responsible for the observed NDR effect which includes flow of extra electrons, heat, and device rupturing that can lead to a drop in the current and transmission function among others; as a result, NDR occurs for such molecular devices. Moreover, molecular devices are sensitive to applied bias, and after a certain amount of applied bias, they break the junction. Similar trends were obtained for the origin of the NDR in  $^7\mathbf{1}_{\text{hshs}}$  (see Figures S5 and S11).

The  $I$ - $V$  plot of  $^3\mathbf{1}_{\text{ls}}$  shows NDR at 0.3 V bias and in the bias region of [0.6, 1.0] V. The transmission spectra and  $p$ DOS were plotted at a bias of 0.2, 0.3, and 0.4 V (see Figures S6 and S8) for both  $\alpha$ - and  $\beta$ -states. It is found that there is only one

peak in the bias window of  $[-0.1, 0.1]$  V at a 0.2 V applied bias with  $T(E) = 0.95$ . However, when a 0.3 V bias voltage is applied through a molecular junction device, no new transmission peak is observed in the bias window as well as  $T(E)$  of the single peak decreases to 0.5, resulting in a decrease in the current, and hence, an NDR characteristic is observed. However, at a 0.4 bias voltage, one more peak at around  $-0.19$  eV to the Fermi energy is observed along with the old peak at 0.1 eV to the Fermi energy, and hence, the current increases again. A similar trend was obtained for  $I_{\downarrow}$  as well. To check the NDR in the region of  $[0.6, 1.0]$  V,  $T(E)$  spectra and corresponding  $p$ DOS (see Figures S7 and S9) were plotted again for both  $\alpha$ - and  $\beta$ -states at all applied bias. In the  $\alpha$ -state, initially, there are two transmission peaks observed in the bias window at a 0.6 applied bias, and their coefficient decreases significantly at a 0.7 V applied bias. These two-peak intensities/magnitudes are smaller at other applied voltages (0.8–1.0 V), and no new peak is observed with a significant transmission coefficient; hence, a net decrease in the current is observed, exhibiting an NDR effect. The same trend was also observed in  $\beta$ -states. In the range of a  $[0.8, 0.9]$  V bias voltage,  $^1\mathbf{I}_{\text{hshs}}$  and  $^7\mathbf{I}_{\text{hshs}}$  exhibit the maximum PVR of 1.95:1 and 1.33:1, respectively. On the other hand,  $^3\mathbf{I}_{\text{ls}}$  shows a PVR of 1.83:1 and 55.65:1 at an applied bias voltage of 0.3 and  $[0.6, 1.0]$  V, respectively. The maximum PVR of around  $\sim 56$  obtained here for the  $^3\mathbf{I}_{\text{ls}}$  state is one of the highest values estimated to date, and it is  $\sim 200\%$  higher than the previous record PVR observed in an organometallic molecular double dot junction.<sup>74</sup> The NDR characteristic of  $^3\mathbf{I}_{\text{ls}}$  with a very high PVR suggests that the studied molecule could be a potential candidate from the applications point of view as a molecular switch, energy harvesting, etc., though stabilization of a low-spin state as the ground state is required, and this can be achieved by incorporation of stronger donor ligands.

In this direction, we modeled complex **1** and modified it with  $[\text{Co}_2(\text{L})(\text{en})_2(\text{ox})_2]$  (en = ethylenediamine, ox = oxalate ion, Figure S13) where the Co(II) centers were found to be stabilize in the desired low-spin state leading to a ferromagnetic coupling between the Co(II) centers ( $J$  value of  $102 \text{ cm}^{-1}$ ), and therefore, such complexes can be the suitable target for the observation of NDR effects with a very high PVR value.

**Effect of Magnetic Exchange and Zero-Field Splitting on Spin Transport Characteristics.** To understand how magnetic exchange and zero-field splitting influence the spin-transport characteristics, we have developed a magneto-structural spin transport correlation for the  $^7\mathbf{I}_{\text{hshs}}$  geometry. At this geometry, the Co–N bond length ( $\sim 2.1 \text{ \AA}$ ) has been symmetrically altered to 1.90  $\text{ \AA}$ , 2.0  $\text{ \AA}$ , 2.2, and 2.3  $\text{ \AA}$ . For each of these geometries, the magnetic exchange coupling constant was computed, and distance dependent  $J$  correlation was developed (see Figure S15(a)). As the distance decreases, the strength of the antiferromagnetic coupling is found to increase ( $-1.31 \text{ cm}^{-1}$  to  $-2.94 \text{ cm}^{-1}$ ), and this is expected due to a stronger orbital overlap at shorter distances. The CASSCF calculations of ZFS calculations reveal that elongation of the Co–N distance was found to enhance the magnitude of the D value ( $+39 \text{ cm}^{-1}$  to  $-79 \text{ cm}^{-1}$ ) changing even the sign from positive to negative (see Figure S15(a) and Table S8(a)). At very long Co–N distances, the geometry resembles that of a distorted tetrahedron which is shown to exhibit a D value in this range.<sup>75</sup> At last, the effect of the change in  $J$  and D and magnetic anisotropy on the  $SFE/I-V$  plot was computed at

two points at Co–N bond lengths of 1.9 and 2.3  $\text{ \AA}$  (see Figure S15(b) and Table S8(b)). It is found that on increasing/decreasing the Co–N bond lengths, the magnitude of  $I_{\uparrow}$  does not alter significantly. However, a significant change in  $I_{\downarrow}$  is noted. At the Co–N bond length of 2.3  $\text{ \AA}$ ,  $I_{\downarrow}$  is found to be similar to the equilibrium geometry; however, when the Co–N bond length is decreased to 1.9  $\text{ \AA}$ ,  $I_{\downarrow}$  increases significantly giving rise to a very high  $SFE$  of around 88%. At this geometry,  $J$  is significantly antiferromagnetic, and D is expected to be large and positive, which lead us to infer that stronger antiferromagnetic coupling could help to facilitate greater  $SFE$ . However, it is essential to acknowledge that the observed changes in  $J$  values are relatively minor, and a comprehensive investigation and further studies are warranted before making more definitive conclusions.

**Correlation to Experiments.** As the transport characteristics of the single molecule junction of **1** are reported, we attempt to correlate the computed data with the experimental observations. (i) The ground state of **1** is found to be the antiferromagnetically coupled state between two  $S = 3/2$  centers of Co(II) with a very weak coupling constant, and our calculations correctly reproduce the ground state; the obtained gap between  $^1\mathbf{I}_{\text{hshs}}$  and  $^7\mathbf{I}_{\text{hshs}}$  correlates well with the experimental  $J$  value estimated from the magnetic data obtained on the prefabricated molecule.

(ii) Further, the molecule optimized at the molecular controlled break junction (MCBJs) device also yields the  $S_{\text{T}} = 0$  ground state, with a stronger antiferromagnetic coupling ( $J = -38 \text{ cm}^{-1}$ ), suggesting the magnetic characteristics of the molecule are also preserved upon fabrication, and this is largely in agreement with the experiments.

(iii) The MCBJs device fabricated using complex **1** exhibits current flowing capacity in the range of 0–20  $\eta\text{A}$  at a lower applied bias voltage. Particularly at the applied bias of 0.5 V, the current experimental capacity of  $\sim 5 \eta\text{A}$  matches the theoretical value of  $\sim 13 \eta\text{A}$ . Although the theoretical value seems overestimated, given the exponential increase in the bias voltage with the applied field and the fact that different break junction devices yield different currents in the experimental setup (type I and type II, see ref 27 for more details), this is reasonable.<sup>27</sup>

(iv) Our calculations unequivocally suggest negative differential resistance (NDR) at both the ground as well as the excited state levels. Particularly, the peak-to-valley ratio (PVR) of 1.95 calculated for the ground state also reasonably matches with the PVR of 1.2 observed in the experimental  $I-V$  plots. Although NDR is clearly visible at all experimental  $I-V$  characteristics at different bias voltages, this has not been substantiated. At 0.7 applied voltage, our calculations predict a sudden inflection in the current flow, and this is also found in the experiments with a substantial increase across various MCBs devices tested, offering confidence in the various properties computed.

## CONCLUSIONS

In summary, spin-state energetics of various exchange-coupled states of  $[\text{Co}_2(\text{L})(\text{hfac})_4]$  (**1**) were evaluated, where the ground state is found to be an antiferromagnetically coupled state between two  $S = 3/2$  centers of Co(II) with a very weak  $J$  value. Both the geometry as well as the weak exchange coupling were found to be largely preserved at the Au interface, validating an important observation that not only is the molecule stable at the interface but also even a very sensitive

parameter such as exchange coupling interaction is not altered significantly upon fabrication. Further, the observed experimental features are solely due to the dimeric nature of **1** and not any other dissociated products.

The computed electronic Hamiltonian parameters from *ab initio* CASSCF/NEVPT2 reveal positive zero-field splitting of  $+39\text{ cm}^{-1}$  for the single-ion anisotropy of Co(II) centers, and this is also found to be largely preserved at the interface geometry ( $D = +30\text{ cm}^{-1}$ , Table S3), validating the observation of pseudo singlet and pseudo triplet  $I-V$  characteristics observed for the dinuclear framework.

The coherent quantum transport calculations performed on various exchange coupled states geometries reveal a significant variation in their spin filtering efficiency, suggesting the underlying exchange coupling constant, the zero-field splitting parameter, and the ligand field, which controls the overall spin-state energy ladder, can fine-tune the transport characteristics. The computed transport characteristics, including the observation of the  $\eta A$  current at low bias, are reproduced in our calculations. Our calculations reveal that the exchange coupled states, both  $S_T = 0$  and  $S_T = 3$  arising from high-spin Co(II) centers, have very similar transport characteristics, and therefore, exchange interaction alone cannot be utilized to fine-tune the *SFE* and *NDR* effects.

Further, interesting features such as negative differential resistance were clearly observed in the calculated transport characteristics of the ground state, and this leads us to relook at the experimental  $I-V$  characteristics where the *NDR* effects are clearly visible, with even the *PVR* computed matching closely with experiments. The partial density of state (*pDOS*) and transmission spectra [ $T(E)$ ] plots reveal that the  $\beta\text{-e}_g$  empty orbitals of the Co(II) center that are responsible for change in conductance and current–voltage ( $I-V$ ) characteristics with the chemical potential of the electrodes at a 0.9 V bias voltage lead to the observance of a significant *NDR* effect. Quite interestingly, the observed voltage at which the *NDR* was observed closely matches the experimental bias at which the current drops.

Our quantum transport studies unveiled a large spin-filtering efficiency of around 44% for complex **1**, albeit for one of its higher excited states ( $S_T = 1$  arising from a ferromagnetic interaction of two low-spin Co(II) centers). The partial density of state and transmission spectra analysis reveal the origin of the large spin-filtering efficiency that arose from a large number of  $\beta\text{-e}_g$  empty orbitals that arise due to magnetic coupling present, and this observation suggests that dinuclear and multinuclear exchange coupled clusters are potential candidates to enhance the *SFE* of molecular devices. The same spin state was also found to exhibit a very strong *NDR* effect with a record *PVR* of  $\sim 56$  noted, the largest for any molecular junction device. We have taken our studies a step further to engineer a molecule that is expected to exhibit a low-spin  $S = 1/2$  spin-state at the Co(II) centers ferromagnetic coupled to each other, and this has resulted in several synthetic targets, if synthesized and fabricated, being potential candidates for data storage, molecular switches, energy harvesting, etc.

## ■ ASSOCIATED CONTENT

### SI Supporting Information

The Supporting Information is available free of charge at <https://pubs.acs.org/doi/10.1021/acs.inorgchem.3c03200>.

Additional figures, optimized geometries, tables containing DFT/*ab initio* calculated parameters, spin-resolved  $T(E)$  and *pDOS* figures, Tables containing  $\alpha/\beta$  current and %*SFE*, spin density plot, molecular orbitals near Fermi energy, and along with the final optimized coordinates for all the species reported (PDF)

## ■ AUTHOR INFORMATION

### Corresponding Authors

Gopalan Rajaraman – Department of Chemistry, IIT Bombay, Powai, Mumbai 400076, India; [orcid.org/0000-0001-6133-3026](https://orcid.org/0000-0001-6133-3026); Email: [rajaraman@chem.iitb.ac.in](mailto:rajaraman@chem.iitb.ac.in)

Biswarup Pathak – Department of Chemistry, IIT Indore, Indore, Madhya Pradesh 453-552, India; [orcid.org/0000-0002-9972-9947](https://orcid.org/0000-0002-9972-9947); Email: [biswarup@iiti.ac.in](mailto:biswarup@iiti.ac.in)

### Authors

Rupesh Kumar Tiwari – Department of Chemistry, IIT Bombay, Powai, Mumbai 400076, India; [orcid.org/0000-0003-3465-1242](https://orcid.org/0000-0003-3465-1242)

Rizwan Nabi – Department of Chemistry, IIT Bombay, Powai, Mumbai 400076, India

Rameshwar L. Kumawat – Department of Chemistry, IIT Indore, Indore, Madhya Pradesh 453-552, India; Present Address: Department of Chemistry, Northwestern University, Evanston, Illinois 60208, United States; [orcid.org/0000-0002-2210-3428](https://orcid.org/0000-0002-2210-3428)

Complete contact information is available at:

<https://pubs.acs.org/10.1021/acs.inorgchem.3c03200>

### Notes

The authors declare no competing financial interest.

## ■ ACKNOWLEDGMENTS

RKT thanks CSIR, and RN thanks IITB for the senior research fellowship (SRF). GR would like to thank DST and SERB (SB/SJF/2019-20/12; CRG/2022/001697) for funding. RLK thanks IIT Indore for SRF. BP thanks CSIR and SERB (01(3046)/21/EMR-II; CRG/2022/000836) for funding.

## ■ REFERENCES

- (1) Bogani, L.; Wernsdorfer, W. Molecular spintronics using single-molecule magnets. In *Nanoscience and technology: a collection of reviews from nature journals*; World Scientific: 2010; pp 194–201.
- (2) Shiraishi, M.; Ikoma, T. Molecular spintronics. *Physica E: Low-dimensional Systems and Nanostructures* **2011**, *43* (7), 1295–1317.
- (3) Wolf, S.; Awschalom, D.; Buhrman, R.; Daughton, J.; von Molnár, v. S.; Roukes, M.; Chtchelkanova, A. Y.; Treger, D. Spintronics: a spin-based electronics vision for the future. *science* **2001**, *294* (5546), 1488–1495.
- (4) Dery, H.; Dalal, P.; Cywiński, Ł.; Sham, L. J. Spin-based logic in semiconductors for reconfigurable large-scale circuits. *Nature* **2007**, *447* (7144), 573–576.
- (5) Xiong, Z.; Wu, D.; Vally Vardeny, Z.; Shi, J. Giant magneto-resistance in organic spin-valves. *Nature* **2004**, *427* (6977), 821–824.
- (6) Di, C. a.; Zhang, F.; Zhu, D. Multi-functional integration of organic field-effect transistors (OFETs): advances and perspectives. *Adv. Mater.* **2013**, *25* (3), 313–330.
- (7) Ishikawa, N.; Sugita, M.; Ishikawa, T.; Koshihara, S.-y.; Kaizu, Y. Mononuclear lanthanide complexes with a long magnetization relaxation time at high temperatures: A new category of magnets at the single-molecular level. *J. Phys. Chem. B* **2004**, *108* (31), 11265–11271.

- (8) Leuenerger, M. N.; Loss, D. Quantum computing in molecular magnets. *Nature* **2001**, *410* (6830), 789–793.
- (9) Sessoli, R.; Gatteschi, D.; Caneschi, A.; Novak, M. Magnetic bistability in a metal-ion cluster. *Nature* **1993**, *365* (6442), 141–143.
- (10) Nabi, R.; Tiwari, R. K.; Rajaraman, G. In silico strategy to boost stability, axiality, and barrier heights in dysprosium SIMs via SWCNT encapsulation. *Chem. Commun.* **2021**, *57* (86), 11350–11353.
- (11) Swain, A.; Tiwari, R. K.; Khatua, M.; Rajaraman, G. Fluxionality Modulating the Magnetic Anisotropy in Lanthanoarene [(ηC<sub>n</sub>R<sub>n</sub>)<sub>2</sub>Ln (II/III)](n= 4–8) Single-Ion Magnets. *Inorg. Chem.* **2023**, *62*, 9552.
- (12) Crivillers, N.; Mas-Torrent, M.; Rovira, C.; Veciana, J. Charge transport through unpaired spin-containing molecules on surfaces. *J. Mater. Chem.* **2012**, *22* (28), 13883–13890.
- (13) Timm, C.; Elste, F. Spin amplification, reading, and writing in transport through anisotropic magnetic molecules. *Phys. Rev. B* **2006**, *73* (23), 235304.
- (14) Haque, F.; Langhirt, M.; Del Barco, E.; Taguchi, T.; Christou, G. Magnetic field dependent transport through a Mn<sub>4</sub> single-molecule magnet. *J. Appl. Phys.* **2011**, *109* (7), 07B112.
- (15) Jo, M.-H.; Grose, J. E.; Baheti, K.; Deshmukh, M. M.; Sokol, J. J.; Rumberger, E. M.; Hendrickson, D. N.; Long, J. R.; Park, H.; Ralph, D. Signatures of molecular magnetism in single-molecule transport spectroscopy. *Nano Lett.* **2006**, *6* (9), 2014–2020.
- (16) Zu, F.-X.; Gao, G.-Y.; Fu, H.-H.; Xiong, L.; Zhu, S.-C.; Peng, L.; Yao, K.-L. Efficient spin filter and spin valve in a single-molecule magnet Fe<sub>4</sub> between two graphene electrodes. *Appl. Phys. Lett.* **2015**, *107* (25), 252403.
- (17) Zu, F.; Liu, Z.; Yao, K.; Gao, G.; Fu, H.; Zhu, S.; Ni, Y.; Peng, L. Nearly perfect spin filter, spin valve and negative differential resistance effects in a Fe<sub>4</sub>-based single-molecule junction. *Sci. Rep.* **2014**, *4* (1), 4838.
- (18) Aravena, D.; Ruiz, E. Coherent transport through spin-crossover single molecules. *J. Am. Chem. Soc.* **2012**, *134* (2), 777–779.
- (19) Gu, Y.; Hu, Y.; Huang, J.; Li, Q.; Yang, J. Spin-Crossover and Coherent Transport Behaviors of a Six-Coordinate Iron (II) Complex with a N<sub>4</sub>O<sub>2</sub> Donor Set. *J. Phys. Chem. C* **2019**, *123* (26), 16366–16372.
- (20) Nihei, M.; Shiga, T.; Maeda, Y.; Oshio, H. Spin crossover iron (III) complexes. *Coord. Chem. Rev.* **2007**, *251* (21–24), 2606–2621.
- (21) Halcrow, M. A. Structure: function relationships in molecular spin-crossover complexes. *Chem. Soc. Rev.* **2011**, *40* (7), 4119–4142.
- (22) Güttlich, P.; Goodwin, H. A.; Garcia, Y. *Spin crossover in transition metal compounds I*; Springer Science & Business Media: 2004; Vol. 1.
- (23) Droghetti, A.; Thielen, P.; Rungger, I.; Haag, N.; Großmann, N.; Stöckl, J.; Stadtmüller, B.; Aeschlimann, M.; Sanvito, S.; Cinchetti, M. Dynamic spin filtering at the Co/Alq<sub>3</sub> interface mediated by weakly coupled second layer molecules. *Nat. Commun.* **2016**, *7* (1), 12668.
- (24) Ramos, A.; Guittet, M.-J.; Moussy, J.-B.; Mattana, R.; Deranlot, C.; Petroff, F.; Gatel, C. Room temperature spin filtering in epitaxial cobalt-ferrite tunnel barriers. *Appl. Phys. Lett.* **2007**, *91* (12), 122107.
- (25) Steil, S.; Großmann, N.; Laux, M.; Ruffing, A.; Steil, D.; Wiesenmayer, M.; Mathias, S.; Monti, O. L.; Cinchetti, M.; Aeschlimann, M. Spin-dependent trapping of electrons at spinterfaces. *Nat. Phys.* **2013**, *9* (4), 242–247.
- (26) Wen, Z.; Zhou, L.; Cheng, J.-F.; Li, S.-J.; You, W.-L.; Wang, X. Spin crossover and high spin filtering behavior in Co-Pyridine and Co-Pyrimidine molecules. *J. Phys.: Condens. Matter* **2018**, *30* (10), 105301.
- (27) Wagner, S.; Kisslinger, F.; Ballmann, S.; Schramm, F.; Chandrasekar, R.; Bodenstern, T.; Fuhr, O.; Secker, D.; Fink, K.; Ruben, M.; et al. Switching of a coupled spin pair in a single-molecule junction. *Nat. Nanotechnol.* **2013**, *8* (8), 575–579.
- (28) Lippert, B. G.; PARRINELLO, J. H.; et al. MICHELE, A hybrid Gaussian and plane wave density functional scheme. *Mol. Phys.* **1997**, *92* (3), 477–487.
- (29) VandeVondele, J.; Krack, M.; Mohamed, F.; Parrinello, M.; Chassaing, T.; Hutter, J. Quickstep: Fast and accurate density functional calculations using a mixed Gaussian and plane waves approach. *Comput. Phys. Commun.* **2005**, *167* (2), 103–128.
- (30) Krack, M. Pseudopotentials for H to Kr optimized for gradient-corrected exchange-correlation functionals. *Theor. Chem. Acc.* **2005**, *114*, 145–152.
- (31) Zhang, Y.; Yang, W. Comment on “Generalized gradient approximation made simple. *Phys. Rev. Lett.* **1998**, *80* (4), 890.
- (32) Stokbro, K. First-principles modeling of electron transport. *J. Phys.: Condens. Matter* **2008**, *20* (6), 064216.
- (33) Bhattacharyya, G.; Kumawat, R. L.; Pathak, B. Porphyrin nanoribbon-based spin filtering devices. *Phys. Chem. Chem. Phys.* **2020**, *22* (28), 16368–16377.
- (34) Bencini, A.; Rajaraman, G.; Totti, F.; Tusa, M. Modeling thiols on Au (111): Structural, thermodynamic and magnetic properties of simple thiols and thiol-radicals. *Superlattices Microstruct.* **2009**, *46* (1–2), 4–9.
- (35) Nabi, R.; Rajaraman, G. Deciphering the origin of variation in the spin ground state and oxidation state of a {Mn 19} cluster on a Au (111) surface: is the Au (111) surface innocent? *Chem. Commun.* **2019**, *55* (57), 8238–8241.
- (36) Frisch, M.; Trucks, G.; Schlegel, H.; Scuseria, G.; Robb, M.; Cheeseman, J.; Scalmani, G.; Barone, V.; Mennucci, B.; Petersson, G. *Gaussian 09*, Revision D.01; Gaussian, Inc.: Wallingford CT, 2009. See also: <http://www.gaussian.com> (accessed 2023-12-10).
- (37) Noodleman, L. Valence bond description of antiferromagnetic coupling in transition metal dimers. *J. Chem. Phys.* **1981**, *74* (10), 5737–5743.
- (38) Neese, F. Software update: the ORCA program system, version 4.0. *Wiley Interdisciplinary Reviews: Computational Molecular Science* **2018**, *8* (1), No. e1327.
- (39) Olsen, J. The CASSCF method: A perspective and commentary. *Int. J. Quantum Chem.* **2011**, *111* (13), 3267–3272.
- (40) Granovsky, A. A. Extended multi-configuration quasi-degenerate perturbation theory: The new approach to multi-state multi-reference perturbation theory. *J. Chem. Phys.* **2011**, *134* (21), 214113.
- (41) Meier, U.; Staemmler, V. An efficient first-order CASSCF method based on the renormalized Fock-operator technique. *Theor. Chim. Acta.* **1989**, *76* (2), 95–111.
- (42) Angeli, C.; Cimiraaglia, R.; Evangelisti, S.; Leininger, T.; Malrieu, J.-P. Introduction of n-electron valence states for multi-reference perturbation theory. *J. Chem. Phys.* **2001**, *114* (23), 10252–10264.
- (43) Angeli, C.; Cimiraaglia, R.; Malrieu, J.-P. N-electron valence state perturbation theory: a fast implementation of the strongly contracted variant. *Chem. Phys. Lett.* **2001**, *350* (3–4), 297–305.
- (44) Angeli, C.; Cimiraaglia, R.; Malrieu, J.-P. n-electron valence state perturbation theory: A spinless formulation and an efficient implementation of the strongly contracted and of the partially contracted variants. *J. Chem. Phys.* **2002**, *117* (20), 9138–9153.
- (45) Soler, J. M.; Artacho, E.; Gale, J. D.; García, A.; Junquera, J.; Ordejón, P.; Sánchez-Portal, D. The SIESTA method for ab initio order-N materials simulation. *J. Phys.: Condens. Matter* **2002**, *14* (11), 2745.
- (46) Brandbyge, M.; Mozos, J.-L.; Ordejón, P.; Taylor, J.; Stokbro, K. Density-functional method for nonequilibrium electron transport. *Phys. Rev. B* **2002**, *65* (16), 165401.
- (47) Xue, Y.; Datta, S.; Ratner, M. A. First-principles based matrix Green’s function approach to molecular electronic devices: general formalism. *Chem. Phys.* **2002**, *281* (2–3), 151–170.
- (48) Di Ventra, M. *Electrical Transport in Nanoscale Systems*; 2008.
- (49) Lee, C.; Yang, W.; Parr, R. G. Development of the Colle-Salvetti correlation-energy formula into a functional of the electron density. *Phys. Rev. B* **1988**, *37* (2), 785.

- (50) Troullier, N.; Martins, J. L. Efficient pseudopotentials for plane-wave calculations. *Phys. Rev. B* **1991**, *43* (3), 1993.
- (51) Büttiker, M.; Imry, Y.; Landauer, R.; Pinhas, S. Generalized many-channel conductance formula with application to small rings. *Phys. Rev. B* **1985**, *31* (10), 6207.
- (52) Liu, X.; Mayer, M. T.; Wang, D. Negative differential resistance and resistive switching behaviors in Cu 2 S nanowire devices. *Appl. Phys. Lett.* **2010**, *96* (22), 223103.
- (53) Chen, J.; Reed, M.; Rawlett, A.; Tour, J. Large on-off ratios and negative differential resistance in a molecular electronic device. *science* **1999**, *286* (5444), 1550–1552.
- (54) Chen, J.; Wang, W.; Reed, M.; Rawlett, A.; Price, D.; Tour, J. Room-temperature negative differential resistance in nanoscale molecular junctions. *Appl. Phys. Lett.* **2000**, *77* (8), 1224–1226.
- (55) Di Ventra, M.; Pantelides, S.; Lang, N. First-principles calculation of transport properties of a molecular device. *Phys. Rev. Lett.* **2000**, *84* (5), 979.
- (56) Kim, W. Y.; Kwon, S.; Kim, K. S. Negative differential resistance of carbon nanotube electrodes with asymmetric coupling phenomena. *Phys. Rev. B* **2007**, *76* (3), 033415.
- (57) Long, M.-Q.; Chen, K.-Q.; Wang, L.; Zou, B.; Shuai, Z. Negative differential resistance induced by intermolecular interaction in a bimolecular device. *Appl. Phys. Lett.* **2007**, *91* (23), 233512.
- (58) Chen, L.; Hu, Z.; Zhao, A.; Wang, B.; Luo, Y.; Yang, J.; Hou, J. Mechanism for negative differential resistance in molecular electronic devices: local orbital symmetry matching. *Phys. Rev. Lett.* **2007**, *99* (14), 146803.
- (59) Hu, L.; Guo, Y.; Yan, X.; Zeng, H.; Zhou, J. Electronic transport properties in [n] cycloparaphenylenes molecular devices. *Phys. Lett. A* **2017**, *381* (25–26), 2107–2111.
- (60) Shi, X.; Zheng, X.; Dai, Z.; Wang, Y.; Zeng, Z. Changes of coupling between the electrodes and the molecule under external bias bring negative differential resistance. *J. Phys. Chem. B* **2005**, *109* (8), 3334–3339.
- (61) Capozzi, B.; Low, J. Z.; Xia, J.; Liu, Z.-F.; Neaton, J. B.; Campos, L. M.; Venkataraman, L. Mapping the transmission functions of single-molecule junctions. *Nano Lett.* **2016**, *16* (6), 3949–3954.
- (62) Huang, J.; Xu, K.; Lei, S.; Su, H.; Yang, S.; Li, Q.; Yang, J. Iron-phthalocyanine molecular junction with high spin filter efficiency and negative differential resistance. *J. Chem. Phys.* **2012**, *136* (6), 064707.
- (63) Majima, Y.; Ogawa, D.; Iwamoto, M.; Azuma, Y.; Tsurumaki, E.; Osuka, A. Negative differential resistance by molecular resonant tunneling between neutral tribenzosubporphine anchored to a Au (111) surface and tribenzosubporphine cation adsorbed on to a tungsten tip. *J. Am. Chem. Soc.* **2013**, *135* (38), 14159–14166.
- (64) Perrin, M. L.; Frisenda, R.; Koole, M.; Seldenthuis, J. S.; Gil, J. A. C.; Valkenier, H.; Hummelen, J. C.; Renaud, N.; Grozema, F. C.; Thijssen, J. M.; et al. Large negative differential conductance in single-molecule break junctions. *Nat. Nanotechnol.* **2014**, *9* (10), 830–834.
- (65) Fan, W.; Zhang, R.; Rocha, A. R.; Sanvito, S. Energy alignment induced negative differential resistance: The role of hybrid states in aromatic molecular devices. *J. Chem. Phys.* **2008**, *129* (7), 074710.
- (66) Xue, Y.; Datta, S.; Hong, S.; Reifenger, R.; Henderson, J. L.; Kubiak, C. P. Negative differential resistance in the scanning-tunneling spectroscopy of organic molecules. *Phys. Rev. B* **1999**, *59* (12), R7852.
- (67) Kang, N.; Erbe, A.; Scheer, E. Observation of negative differential resistance in DNA molecular junctions. *Appl. Phys. Lett.* **2010**, *96* (2), 023701.
- (68) Galperin, M.; Ratner, M. A.; Nitzan, A. Hysteresis, switching, and negative differential resistance in molecular junctions: a polaron model. *Nano Lett.* **2005**, *5* (1), 125–130.
- (69) Chappert, C.; Fert, A.; Van Dau, F. N. The emergence of spin electronics in data storage. *Nat. Mater.* **2007**, *6* (11), 813–823.
- (70) Donhauser, Z.; Mantooth, B.; Kelly, K.; Bumm, L.; Monnell, J.; Stapleton, J. J.; Price, D., Jr.; Rawlett, A.; Allara, D.; Tour, J.; et al. Conductance switching in single molecules through conformational changes. *Science* **2001**, *292* (5525), 2303–2307.
- (71) Guo, Y.-D.; Zeng, H.-L.; Hu, L.-Z.; Yan, X.-H.; Mou, X.-Y.; Yang, M.-S. Multiple spin-resolved negative differential resistance and electrically controlled spin-polarization in transition metal-doped [6] cycloparaphenylenes. *Phys. Lett. A* **2018**, *382* (38), 2763–2768.
- (72) Tao, L.; Wang, J. Giant magnetoresistance and perfect spin filter effects in manganese phthalocyanine based molecular junctions. *Nanoscale* **2017**, *9* (34), 12684–12689.
- (73) Prasongkit, J.; Grigoriev, A.; Pathak, B.; Ahuja, R.; Scheicher, R. H. Transverse conductance of DNA nucleotides in a graphene nanogap from first principles. *Nano Lett.* **2011**, *11* (5), 1941–1945.
- (74) Liu, R.; Ke, S.-H.; Baranger, H. U.; Yang, W. Negative differential resistance and hysteresis through an organometallic molecule from molecular-level crossing. *J. Am. Chem. Soc.* **2006**, *128* (19), 6274–6275.
- (75) Sarkar, A.; Dey, S.; Rajaraman, G. Role of Coordination Number and Geometry in Controlling the Magnetic Anisotropy in FeII, CoII, and NiII Single-Ion Magnets. *Chem.—Eur. J.* **2020**, *26* (62), 14036–14058.